Morphology and strain of self-assembled semipolar GaN quantum dots in $(11\bar{2}2)$ AlN

G. P. Dimitrakopulos,[1,a)] E. Kalesaki,[1] J. Kioseoglou,[1] Th. Kehagias,[1] A. Lotsari,[1] L. Lahourcade,[2] E. Monroy,[2] I. Häusler,[3] H. Kirmse,[3] W. Neumann,[3] G. Jurczak,[4] T. D. Young,[4] P. Dłużewski,[4] Ph. Komninou,[1] and Th. Karakostas[1]

[1]*Department of Physics, Aristotle University of Thessaloniki, GR 54124 Thessaloniki, Greece*
[2]*CEA-CNRS Group "Nanophysique et Semiconducteurs," INAC/SP2M/NPSC, CEA-Grenoble, 17 rue des Martyrs, 38054 Grenoble, Cedex 9, France*
[3]*Institut für Physik, Humboldt-Universität zu Berlin, AG Kristallographie, Newtonstrasse 15, D-12489 Berlin, Germany*
[4]*Institute of Fundamental Technological Research of the Polish Academy of Sciences, ul. Pawińskiego 5b, 02-106 Warsaw, Poland*

GaN quantum dots (QDs) grown in semipolar $(11\bar{2}2)$ AlN by plasma-assisted molecular-beam epitaxy were studied by transmission electron microscopy (TEM) and scanning transmission electron microscopy techniques. The embedded $(11\bar{2}2)$-grown QDs exhibited pyramidal or truncated-pyramidal morphology consistent with the symmetry of the nucleating plane, and were delimited by nonpolar and semipolar nanofacets. It was also found that, in addition to the $(11\bar{2}2)$ surface, QDs nucleated at depressions comprising $\{10\bar{1}1\}$ facets. This was justified by *ab initio* density functional theory calculations showing that such GaN/AlN facets are of lower energy compared to $(11\bar{2}2)$. Based on quantitative high-resolution TEM strain measurements, the three-dimensional QD strain state was analyzed using finite-element simulations. The internal electrostatic field was then estimated, showing small potential drop along the growth direction, and limited localization at most QD interfaces. © *2010 American Institute of Physics*. [doi:10.1063/1.3506686]

I. INTRODUCTION

Intensive research efforts in the field of III-nitride semiconductor optoelectronic devices are concentrated in the extension of their operational range from the deep ultraviolet to the infrared wavelengths. Although such feat can in principle be achieved through alloying based on the bandgaps of the binary compound constituents (AlN, GaN, and InN), the practically accessible spectral range is reduced in the conventional polar [0001]-grown heterostructures. This is due to the polarization-induced internal electric field that leads to carrier separation and band structure distortion in heterostructures, thus reducing significantly the internal quantum efficiency and causing a photoluminescence redshift [the quantum-confined Stark effect (QCSE)].[1] Nonpolar and semipolar growth orientations are investigated in order to diminish the effect of the internal electric field.[2–5]

So far the heteroepitaxial growth of nonpolar and semipolar III-nitrides on sapphire results in large threading dislocation (TD) densities that promote nonradiative electron-hole recombination. This is attributed to the defect content and anisotropic behavior of the heteroepitaxial interfaces.[6–8] A way to reduce the nonradiative recombination rate in semiconductors with high defect densities consists in profiting from the three-dimensional (3D) electron confinement in quantum dot (QD) nanostructures.[9,10] In a recent contribution, we have demonstrated the synthesis of self-assembled GaN QDs in semipolar $(11\bar{2}2)$ AlN by plasma-assisted molecular-beam epitaxy (PAMBE).[11] A modified Stranski–Krastanow growth mode was achieved by gallium-rich growth of a few GaN monolayers (MLs) followed by a growth interruption in vacuum. Photoluminescence (PL) spectroscopy and time-resolved PL measurements confirmed the reduction in the QCSE and the 3D carrier confinement.

The present contribution focuses on the elucidation of the morphology, strain state, and internal electric field of GaN QDs embedded in $(11\bar{2}2)$ AlN. Previous such studies of nonpolar QDs have shown that the built-in electric field depends critically on QD shape and size, and on the QD/matrix interfaces.[12–14] The identification of the QD facets is of special importance since the polarization-induced charge at the interface depends on the angle between the facet and the polar *c*-axis.

In this work, transmission electron microscopy (TEM), high-resolution TEM (HRTEM), and scanning-TEM (STEM) observations were employed for the experimental determination of the QD morphology. Quantitative analysis of HRTEM (qHRTEM) observations yielded experimental nanoscale measurements of the strain state in the QDs in two-dimensional (2D) projections. These experimental results were compared to finite-element (FE) calculations in order to estimate the 3D strain distribution and the internal electric field. *Ab initio* density functional theory (DFT) calculations

a)Electronic mail: gdim@auth.gr.

of interfacial energy were implemented in order to compare principal interfaces of the QDs.

II. EXPERIMENTS

Superlattices consisting of 20 periods of GaN QDs embedded in 10 nm AlN spacers were grown by PAMBE on a 170 nm $(11\bar{2}2)$ AlN layer deposited on *m*-plane sapphire.[11] The substrate temperature was 730 °C and the nitrogen-limited growth rate was 0.3 ML/s (270 nm/h). The QDs were synthesized by growth of 2D GaN layers under gallium-rich conditions, followed by a 90 s growth interruption in vacuum. Samples of different GaN amount in the QD layers were investigated, i.e., the equivalent thickness of the GaN layers was 5 and 10 ML. The growth mode of GaN on AlN was analyzed *in situ* by reflection high-energy electron diffraction (RHEED).

Cross sectional TEM specimens along the $[0001]_{Al_2O_3}$ and $[\bar{1}\bar{1}20]_{Al_2O_3}$ directions, as well as plan-view specimens were prepared by mechanical polishing followed by precision Ar$^+$ ion-milling. Conventional TEM (CTEM) and HR-TEM observations were implemented using a 200 kV TEM JEOL 2011 microscope (0.19 nm point resolution, Cs =0.5 mm). High-angle annular dark field Z-contrast images were recorded using a 200 kV FEG TEM/STEM JEOL JEM2200FS microscope. QHRTEM of the QD strain state was performed by geometrical phase analysis (GPA).[15,16] For this purpose, HRTEM images were digitized at 4000 dpi resolution using a special purpose scanner.

III. EXPERIMENTAL RESULTS

Selected-area electron diffraction showed that the AlN template exhibited the established orientation relationship with sapphire i.e., $(11\bar{2}2)_{AlN}\|(1\bar{1}00)_{Al_2O_3}$, $[\bar{1}\bar{1}23]_{AlN}\|[0001]_{Al_2O_3}$, $[1\bar{1}00]_{AlN}\|[\bar{1}\bar{1}20]_{Al_2O_3}$.[17] The specimens had upward (metal-polar) sense of the inclined *c*-axis as determined by convergent-beam electron diffraction.

Figure 1 shows overall cross-sectional CTEM and Z-contrast STEM images of the QD heterostructure of the 10 ML sample. It is seen that the QD superlattices were distorted by the large density of extended defects (TDs and stacking faults) contained in the MBE-grown template. The defects introduced roughening and depressions at the GaN/AlN interface, causing many QDs to grow partially on inclined crystallographic planes. However, the great majority of QDs sat on the $(11\bar{2}2)$ plane, and the QDs were epitaxial with the $(11\bar{2}2)$ matrix.

The QD dimensions were measured from cross-sectional HRTEM and Z-contrast STEM images along $[\bar{1}\bar{1}23]_{AlN}$ and $[1\bar{1}00]_{AlN}$. About thirty QDs in total were measured for each sample. In the 5 ML sample, the average projected width of QD base and height were 10.9 ± 1.1 nm and 2.8 ± 0.6 nm, respectively. In the 10 ML sample an increase was observed, i.e., the corresponding values were 21.0 ± 5.0 nm 4.8 ± 1.0 nm for QD width and height, respectively. Hence the average QD size was found to increase with increasing the amount of deposited GaN. The larger distribution of mea-
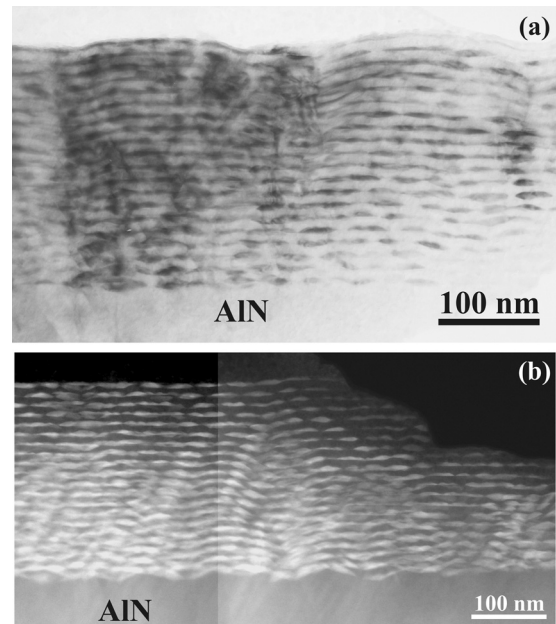

FIG. 1. (a) Bright-field CTEM image along the $[\bar{1}\bar{1}23]$ zone axis and (b) Z-contrast STEM image along $[1\bar{1}00]$ of the overall GaN QD heterostructure of the 10 ML sample grown on semipolar $(11\bar{2}2)$ AlN template. The heterostructure is perturbed by TDs, and depressions are observed at the GaN/AlN interface.

sured QD widths for the 10 ML sample could be attributed to the fact that larger QD volumes have higher probability of being cut by the TEM foil surfaces and hence be partially included in the specimen. In both samples, the AlN spacers between the QD layers were observed to have a thickness of 10 nm approximately, measured between the QD bases.

Regarding the planar density of QDs, previous AFM surface measurements of uncapped nominally 5 ML thick GaN QD layers were compared to the density of similar buried QDs estimated by plan-view Z-contrast STEM observations.[11] Such a Z-contrast image is illustrated in Fig. 2. Measurements in plan-view images were performed in a net area of 0.3 μm^2 and the determined average QD planar density was $(1.3\pm0.7)\times10^{11}$ cm^{-2}. This value is larger than the value of $\sim0.5\times10^{11}$ cm^{-2} reported by AFM,[11] and
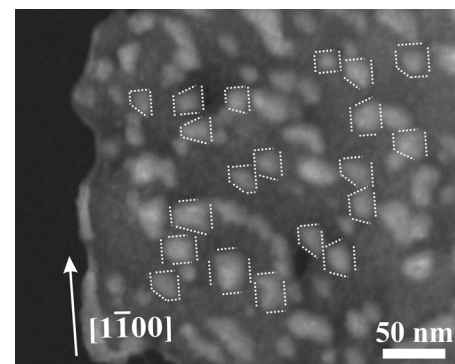

FIG. 2. Plan-view Z-contrast STEM images along $[22\bar{4}3]$, obtained from the 5 ML sample, showing GaN QDs with rectangular and trapezoidal-like projected shapes. The orientation of the in-plane $[1\bar{1}00]$ axis is indicated, and dotted lines have been drawn around some QDs to aid the eye regarding shape determination.
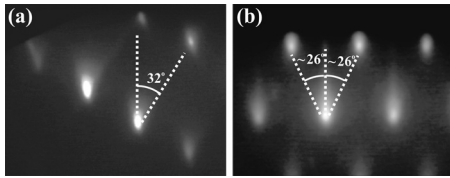
FIG. 3. RHEED patterns with the electron beam (a) along the $[1\bar{1}00]$ and (b) $[\bar{1}\bar{1}23]$ azimuths. Extra spots in the patterns correspond to the QD lateral facets, i.e., $(11\bar{2}0)$ in (a), and the $\{10\bar{1}1\}$ crystallographically equivalent facets, in (b).

could be attributed to the thickness of the plan-view TEM specimen. Despite that measurements were obtained adjacent to the edge of the TEM sample, the thickness of the spacers between the QD layers is too small (~10 nm) and hence it can be estimated that approximately two QD layers must be included in the image. Hence the QD density may be over-estimated by a factor of two. On the other hand, as discussed in Ref. 11, the AFM measurement could underestimate the QD density since its resolution is limited by the tip size, and QDs that are close together may not be resolved as separate surface features. For the 10 ML sample, the QD density de-termined by TEM was $(3.0\pm1.1)\times10^{11}$ cm^{-2}.

Figure 2 is a plan-view Z-contrast STEM image showing that most QD morphologies are projected as rectangular or trapezoidal shapes, as indicated by dotted lines. This Z-contrast image has been obtained along the $[22\bar{4}3]$ zone axis inclined at 6.7° relative to the normal to the $(11\bar{2}2)$ plane. Note that in the hexagonal lattice, the direction normal to the $(11\bar{2}2)$ plane is $[11\bar{2}(2/\Lambda^2)]$, where $\Lambda=(2/3)^{1/2}$ (c/a).[18] Regarding the side facets of the QDs, Fig. 3 illus-trates RHEED patterns, obtained after the growth interrup-tion stage. Patterns obtained along the $[\bar{1}\bar{1}23]$ and $[1\bar{1}00]$ azimuths showed additional reflections due to diffraction from the $(11\bar{2}0)$ and $\{10\bar{1}1\}$ QD facet planes, respectively. This was further confirmed from the HRTEM observations. Figure 4 is a cross-sectional HRTEM image along the $[\bar{1}\bar{1}23]$ zone axis. It is seen that the side facets of the QDs are aligned with the $\{10\bar{1}1\}$ edge-on planes that form angles of 26° with the $(11\bar{2}2)$ plane. Another possible plane orientation for these side facets is the $\{10\bar{1}2\}$ which is inclined in this projection and forms an angle of 27.4° with the $(11\bar{2}2)$. The
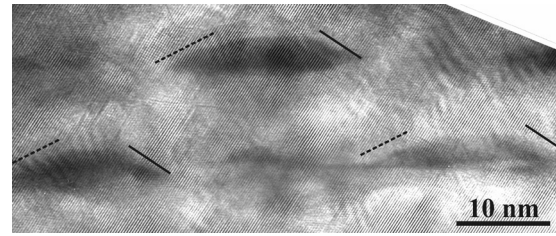

FIG. 5. Cross sectional HRTEM image of $(11\bar{2}2)$ GaN QDs in the 10 ML sample, observed along $[1\bar{1}00]$. The $(11\bar{2}0)$ side facets are indicated by solid lines. The dashed lines indicate facets of average orientation $(11\bar{2}5)$ or $(11\bar{2}6)$.

QDs were either pyramidal-shaped or truncated at their top. For example, in Fig. 4 the QD on the right hand-side is pyramidal while the QD on the left is truncated at the top. The middle QD has nucleated on a depression of the surface and exhibits $\{10\bar{1}1\}$ truncation at its base.

In the HRTEM image of Fig. 5 the QDs are shown viewed along $[1\bar{1}00]$. In this projection direction only the (0002) basal planes are resolved. Still, it can be seen that the QDs exhibit a sharper facet, indicated by solid lines on the right-hand side, whereas they are more lenticular-shaped on the left-hand side (dashed lines). The right-hand side nano-facets appear to be perpendicular to the basal planes, making them consistent with the $(11\bar{2}0)$ orientation. Regarding the left-hand side, the average interfacial orientation varied be-tween $\sim25°-30°$. Hence the planes $(11\bar{2}5)$ or $(11\bar{2}6)$ were assigned on average. In the QDs depicted in Fig. 5 the trun-cation at their top is evident. From Figs. 4 and 5, it can also be observed that the QDs exhibited rather similar dimensions in the two projection directions, owing probably to the low energy GaN/AlN side facets. This is in contrast to the case of nonpolar a-plane GaN QDs which showed pronounced shape asymmetry.[14]

Based on the assigned crystallographic planes, Fig. 6 illustrates the resulting delimiting geometrical shapes of the $(11\bar{2}2)$ QDs. When two crystallographically equivalent fac-ets, $\{10\bar{1}1\}$ or $\{10\bar{1}2\}$, coexist, the QD shape exhibits mirror symmetry consistent with the $(1\bar{1}00)$ glide-mirror plane of wurtzite that is perpendicular to the $(11\bar{2}2)$ plane. Alterna-tively, one $\{10\bar{1}1\}$ and one $\{10\bar{1}2\}$ facet may coexist in the
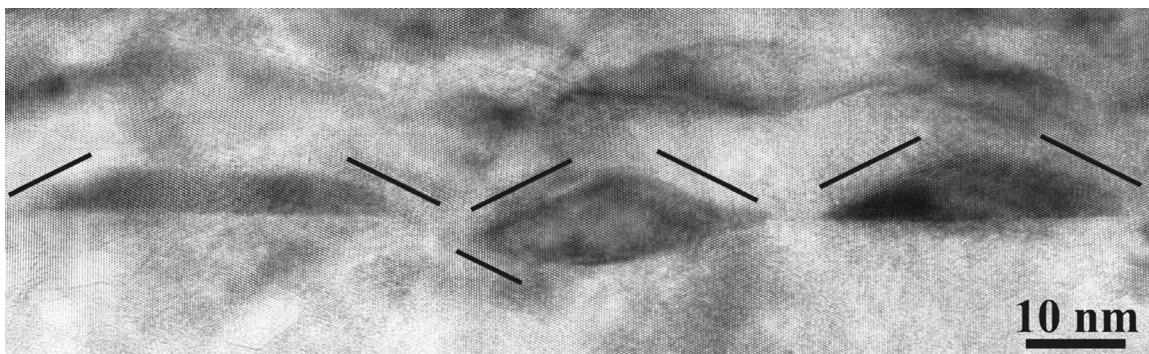

FIG. 4. Cross sectional HRTEM image of $(11\bar{2}2)$ GaN QDs in the 10 ML sample, observed along $[\bar{1}\bar{1}23]$. The facets indicated by solid lines are of $\{10\bar{1}1\}$ type.
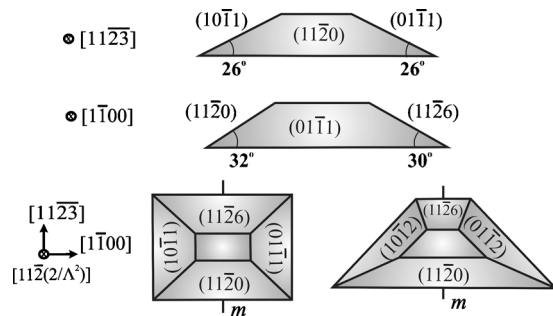
FIG. 6. Schematic illustration, along three perpendicular projection directions, of the two delimiting QD morphologies of the $(11\bar{2}2)$-nucleated QDs. The orientation of the $(1\bar{1}00)$ glide mirror plane is indicated.

same QD, leading to two variants of the QD shape due to the suppression of the mirror symmetry. The proposed delimiting morphologies are consistent with the plan-view observation of rectangular or trapezoidal shapes given in Fig. 2. Also, in Fig. 2 the QDs are correctly oriented relative to the in-plane $[1\bar{1}00]$ direction.

Irregularities of the QD shapes appeared due to the truncations caused by nucleation on surface depressions. This is illustrated for example by the QD at the center of Fig. 4. Overall, the orientations of the inclined facets forming the depressions were measured in projection along the $[\bar{1}\bar{1}23]$ zone axis, and it was determined that they were consistent with the $\{10\bar{1}1\}$ orientations. It is interesting that the $\{10\bar{1}1\}$ interfaces appeared both as facets of the QDs as well as at the depressions of the film. Facets of type $\{10\bar{1}1\}$ have been observed previously at V-defects formed at the surface terminations of TDs, as well as at GaN sidewalls in lateral epitaxial overgrowth.[19–23]

In a consistent manner, when the specimens where viewed along the $[1\bar{1}00]$ zone axis, the $(11\bar{2}0)$ truncation was found to be dominant. Figure 7(a) depicts part of the region shown in Fig. 1(b), and illustrates QDs nucleated at $(11\bar{2}0)/(11\bar{2}2)$ facet junctions and stacked one on top of the other. In the high resolution STEM image of Fig. 7(b) the (0002) basal planes are visible, and they are seen to be normal to the $(11\bar{2}0)$ facets as expected. By comparing Figs. 7(a) and 7(b), it is also seen that the vertical stacking of these QDs follows approximately the inclination of the basal plane. Hence it is likely to have been caused by an ascending TD with its line direction on the basal plane or due to the morphology formation of a macro-step in the AlN barrier layer just above the island which then constitutes a favorable nucleation site for the next GaN island. The irregularity of truncations due to the interfacial roughness contributes to the shape variations observed in plan-view (Fig. 2).

Further cross-sectional two-beam CTEM and HRTEM observations were carried out in order to clarify whether the TDs are a primary cause of the local stacking of QDs along the orientation of the basal plane. Figure 8(a) is a weak-beam CTEM image of the 10 ML sample obtained off the $[1\bar{1}00]$ zone axis with a **g**/3**g** condition using **g** 0002. Under this observation condition, TDs with a Burgers vector component along the c-axis are visible. These can be lattice dislocations
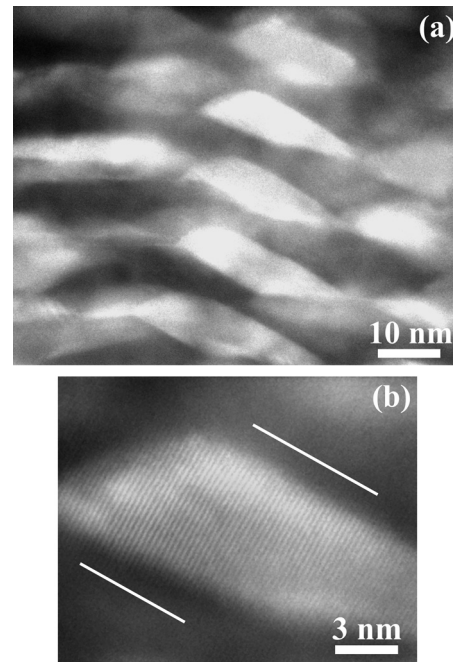

FIG. 7. (a) Z-contrast STEM image showing QDs nucleated at $(11\bar{2}0)/(11\bar{2}2)$ facet junctions. (b) High resolution STEM image of one of the QDs depicted in (a). The fringes corresponding to the basal planes are seen to be vertical to the $(11\bar{2}0)$ facets indicated by white solid lines.

or Frank partials around I_1 stacking faults (SFs) .[24] In Fig. 8(a) one row of QDs stacked along the basal plane is well-discernible because it becomes brighter under this diffraction condition, and can be seen to be associated to ascending TDs. The AlN/sapphire interfaces comprised a zone of misoriented nanocrystals manifested by Moiré fringes and described in detail elsewhere.[8] Such nanocrystals act as TD sources.[7] The influence of TDs on the QD stacking and morphology can also be seen in greater detail in the cross-sectional HRTEM image of Fig. 8(b) obtained from the 5 ML sample along the $[\bar{1}\bar{1}23]$ zone axis. At least two TDs are discernible in the image and they are seen to be associated with the introduction of $\{10\bar{1}1\}$ facets where QDs nucleate preferentially. The TD-induced introduction of $\{10\bar{1}1\}$ facets in III-nitrides, for example at V-defects, is well-established in the literature.[22,23]

Figure 8(b) also serves to illustrate the existence of a clearly resolved 2D wetting layer (WL) in the case of the 5 ML sample. The WL appears to be discontinuous at some points. This discontinuity could be attributed to local diffusion caused by the strain fields of the TDs but also another reason is the zone axis of observation. At the horizontal parts of the WL the contrast is weaker because there is no first-order Bragg reflection parallel to the growth direction and so the mass contrast due to absorption is not directly enhanced by contrast due to the biaxial strain in the lattice planes. On the other hand, when the WL becomes parallel to lattice planes that introduce first-order Bragg reflections, such as the $\{10\bar{1}1\}$ planes, the strain contribution is much more pronounced and hence the WL becomes better discernible. Regarding the 10 ML sample the WL was not so well discern-
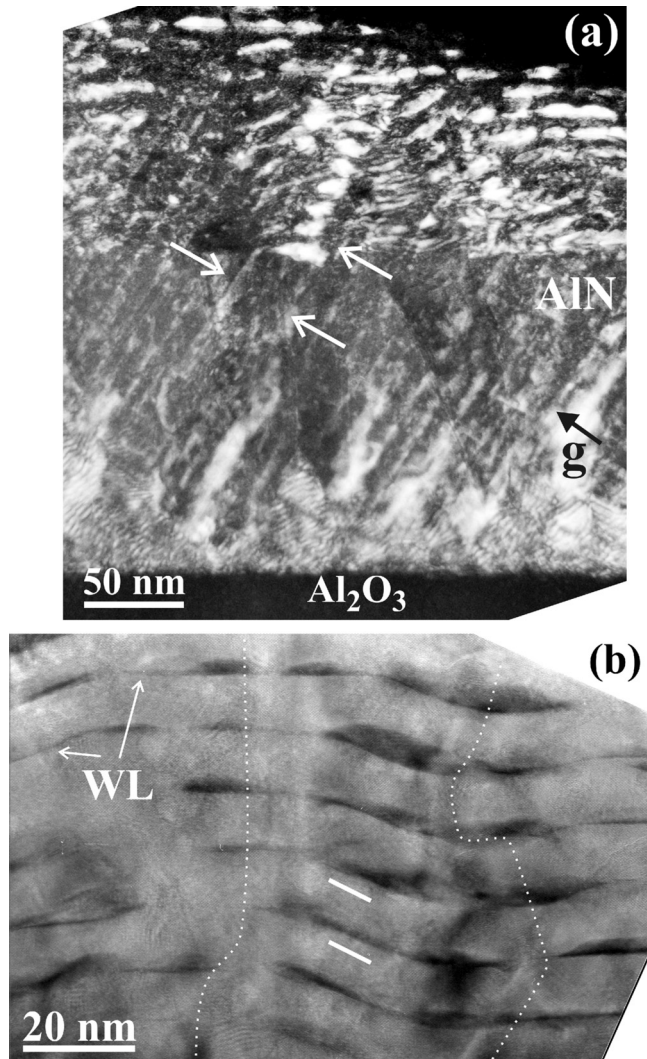
FIG. 8. (a) Cross-sectional **g**/3**g** weak-beam CTEM image of the 10 ML sample obtained off the $[1\bar{1}00]$ zone axis using **g** 0002. Inclined TDs are discernible as well as a row of QDs stacked along the basal plane and indicated by an arrow. Other arrows indicate TDs that appear to be associated with this row of QDs. (b) Cross sectional HRTEM image of the 5 ML sample, obtained along $[\bar{1}\bar{1}23]$, and showing a region with at least two ascending TDs, indicated by dotted lines. The region is seen to comprise $(10\bar{1}1)$ facets where QDs have nucleated. The orientation of the $(10\bar{1}1)$ planes is indicated by solid white lines. The WL between the QDs is also well-resolved, as indicated by arrows.

ible by HRTEM as in the case of the 5 ML sample. This is due to the higher QD density and larger QD size that caused the contrast of the WL to be overlapped.

In order to elucidate the strain state of the $(11\bar{2}2)$ QDs, HRTEM images were analyzed by GPA. Figure 9(a) shows the HRTEM image of a QD along the $[\bar{1}\bar{1}23]$ zone axis, from which a 2D projection of the strain field was obtained. The QD is localized close to the edge of the TEM specimen, where the foil thickness is approximately 5 nm. This image does not exhibit local changes in the defocus condition making it suitable for strain analysis. For this purpose the resolution of the digitized image was scaled down to 2048 dpi. The projection of the strain field along the zone axis was generated by employing the **g** $01\bar{1}1$ and **g** $10\bar{1}1$ spatial frequencies in the diffractogram obtained from the HRTEM im-
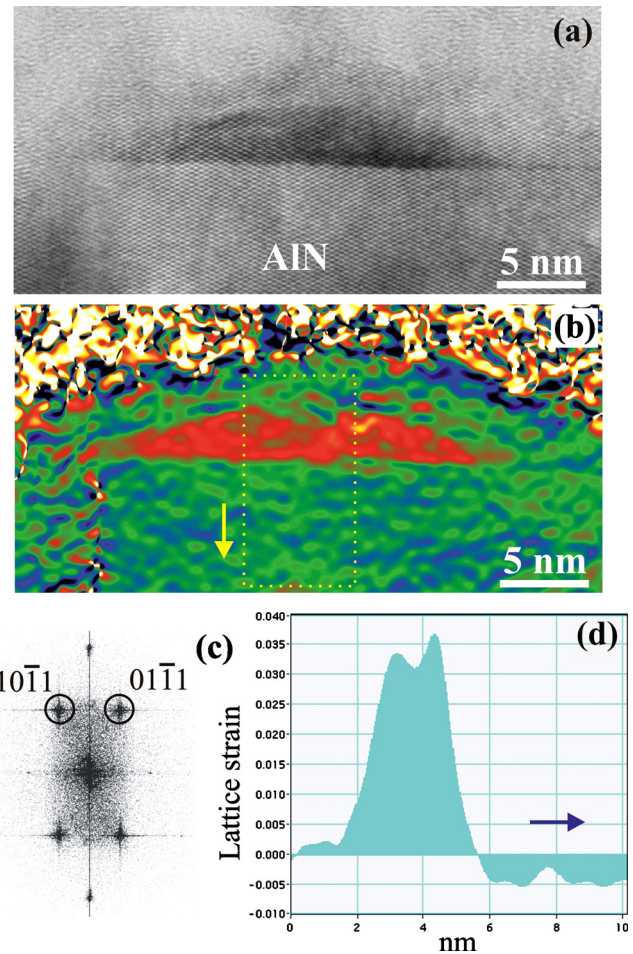

FIG. 9. (Color online) (a) Cross sectional HRTEM image of a $(11\bar{2}2)$-nucleated QD observed along $[\bar{1}\bar{1}23]$. (b) Corresponding lattice strain map along the growth direction obtained with 0.71 nm spatial resolution ($g/3$ mask size). (c) FFT of the HRTEM image of (a). The spatial frequencies employed for the GPA strain analysis are indicated. (d) Lattice strain profile along the growth direction. The profile was obtained using 6 nm integration width from the area indicated in (b). The spatial resolution for the particular profile was 0.95 nm ($g/4$ mask size), and the accuracy of strain determination was 0.4%.

age by fast Fourier transform (FFT). Two mask sizes were employed, namely $g/3$ and $g/4$, corresponding to spatial resolutions of strain field determination equal to 0.71 nm and 0.95 nm, respectively. Figure 9(b) illustrates the resulting map of the lattice strain component along the growth direction, obtained using $g/3$ mask size and having as reference the AlN matrix [i.e., it is the reduced relative variation in the interplanar spacing $(d_{GaN}-d_{AlN})/d_{AlN}$]. A depression of the strain at the QD's upper central region is noted. Figure 9(c) is the diffractogram of Fig. 9(a) showing the employed spatial frequencies. Figure 9(d) illustrates the strain profile along the growth direction, obtained from the central part of the QD using an integration width of 6 nm. The average value of the strain there was 3.4%. The best accuracy of strain determination, attained with a $g/4$ mask, was 0.4%.

IV. FE ANALYSIS OF THE ELASTIC-ELECTRIC QD BEHAVIOR

The elastic strain state of QDs is extremely important to assess piezoelectric effects and thus evaluate the built-in po-

larization potential and the charge carrier separation.[25,26] The complexity of the QD shape does not allow a simple biaxial approximation of the strain state, since the presence of multiple facets and the small embedded volume size can lead to considerable deviations.[27,28] Furthermore, in order to accurately correlate to qHRTEM experimental measurements, the influence of the TEM foil thickness on the measured strain must be taken into account. In order to achieve electron transparency suitable for HRTEM observations, the TEM foil thickness may be smaller than the maximum thickness of the QDs (i.e., the thickness at their base); this is the case in Fig. 9. In order to take into account correctly these strain effects, FE analysis was undertaken. Continuum-based strain calculations were performed for the (11$\bar{2}$2) QDs, and were compared to the qHRTEM experimental observations.

There are two predominant fields affecting the optoelectronic properties of the QDs. First, there is the elastic displacement field u_i, appearing as a result of lattice mismatch in a heterostructure, which leads to the appearance of stress σ_{ij}. The second field is the electric displacement field D_i, which leads to the appearance of the built-in electric potential V. To calculate the elastic-electric problem the following coupled equation set must be solved:[29]

$$\sigma_{ij} = C_{ijkl}(\varepsilon_{kl}^{lt} - \varepsilon_{kl}^{ch}) - e_{ijk}\partial_k V, \tag{1a}$$

$$D_i = e_{ijk}(\varepsilon_{jk}^{lt} - \varepsilon_{jk}^{ch}) + \mu_{ij}\partial_j V + P_i^{spont}, \tag{1b}$$

where i, j, k, $l = 1, 2, 3$; C_{ijkl} is the fourth-order tensor of stiffness moduli, e_{ijk} is the third-order piezoelectric tensor, μ_{ij} is the second-order diagonal dielectric tensor, and P_i^{spont} is the spontaneous polarization moduli arranged in a vector form. The lattice (total) strain tensor $\boldsymbol{\varepsilon}^{lt}$ is composed of an elastic part $\boldsymbol{\varepsilon}^e$ ($\boldsymbol{\varepsilon}^e = \boldsymbol{\varepsilon}^{lt} - \boldsymbol{\varepsilon}^{ch}$) and a chemical part $\boldsymbol{\varepsilon}^{ch}$. The latter corresponds to the lattice mismatch and is purely diagonal ($i \equiv j$), i.e.,

$$\varepsilon_{ii}^{ch} = (a_i^{GaN} - a_i^{AlN})/a_i^{AlN}, \tag{2}$$

where $a_1 = a_x = a$, $a_2 = a_y = a$, and $a_3 = a_z = c$ with a and c being the lattice parameters of the wurtzite structure. Material properties of wurtzite GaN and AlN crystals were taken from the paper of Vurgaftman *et al.*[30]

In our approximation, equation set (1) was solved in a semicoupled manner, i.e., the inverse piezoelectric coupling was ignored in Eq. (1a) by setting **e** = 0. This coupling is expected to be slight and not to affect our main results for stress-strain distribution. The implemented scheme is equivalent to solving at the first step the elastic Eq. (1a); next, for the resultant strain/stress distribution, the electric Eq. (1b) is solved. Nonlinear elasticity theory based on the use of the logarithmic strain measure was implemented.[31] Boundary conditions were determined under the scheme of Multipoint Constraints in order to take into account the influence of the neighboring QDs. Under this approach, the external faces of the FE model are allowed to move normal to their surface (but remain flat), to accommodate elastic relaxation in the QD and its surroundings. In this description, elastic relaxation of the GaN QD causes slight expansion of AlN matrix in addition to the local interaction between QD and matrix near interfaces. Tensor transformation law was implemented

in order to determine the tensor elements and the induced elastic-electric field for the semipolar orientation at hand, considering their projection in a rotated coordinate system.

The principal motivation for employing FE method is for the relative ease with which one can construct arbitrary geometries with the space grid. The 3D FE grid that describes the geometry of the rectangular-based (11$\bar{2}$2)-nucleated QD is given in Fig. 10(a), and comprised a QD with lengths of base edges equal to 20 nm along [1$\bar{1}$00], and 18 nm along [$\bar{1}\bar{1}$23]. The QD height was 3.5 nm. After relaxation, a nonuniform elastic strain distribution was observed in the QD, exhibiting highest strain values at the junctions between the base and the side facets [Figs. 10(b) and 10(c)]. Depression of the QD strain was found close to the upper (11$\bar{2}$2) facet at the junctions with the side facets. Comparing with the experimental map of Fig. 9(b), the depression of the strain at the upper (11$\bar{2}$2) facet is in satisfactory agreement. However, pronounced strain was not observed experimentally at the junctions between base and side facets, and this can be attributed to these junctions not being sharp.

The spontaneous polarization and elastic-electric coupling are known to be fundamental criteria governing electron–hole confinement properties in non-polar QDs,[25] and their influence was found to be equally important in semipolar QDs. While a homogeneous potential distribution was predicted on the [$\bar{1}\bar{1}$23] projection, due to the symmetry of the QDs in this projection direction [Fig. 10(d)], a significant rotation in the localization of positive and negative components of the electrostatic potential was predicted along [1$\bar{1}$00] [Fig. 10(e)]. Along the [1$\bar{1}$00] direction, the spatial distribution of the positive and negative localizations was affected by the orientations of the corresponding side facets. In particular, the positive region was sharply defined, whereas the negative region was spread out. This is explained by the fact that the (11$\bar{2}$6) facet of the QD is inclined at ~62° to the polar axis. On the other hand, the potential peaks negatively on the (11$\bar{2}$0) QD facet where the polar c-axis lies in-plane. This results in weaker charge localization.

Figure 11 illustrates line scans of elastic and lattice strain, as well as polarization potential, obtained through the QD's center along the growth direction (z-axis). The elastic strain [Fig. 11(a)] revealed slight expansion in the z-direction, while along the x and y directions the strain was compressive. Regarding the lattice strain, expressed with respect to relaxed AlN, the magnitude of ε_{zz}^{lt} was considerably higher than the other components [Fig. 11(b)]. Moreover, it was higher than the nominal lattice mismatch for this particular direction, which is 2.9%. In particular, 3.7% was obtained at the center of the QD. In order to take into account the effect of the estimated TEM foil thickness, we truncated the FE model space (thinning down) to 6 nm thickness along the [$\bar{1}$1$\bar{2}$3] projection direction, which resulted in a decrease in the strain at the QD center. This decrease, averaged through the thickness of the sample, was ~10%. The final result is in good agreement with the qHRTEM measurement of Fig. 9.
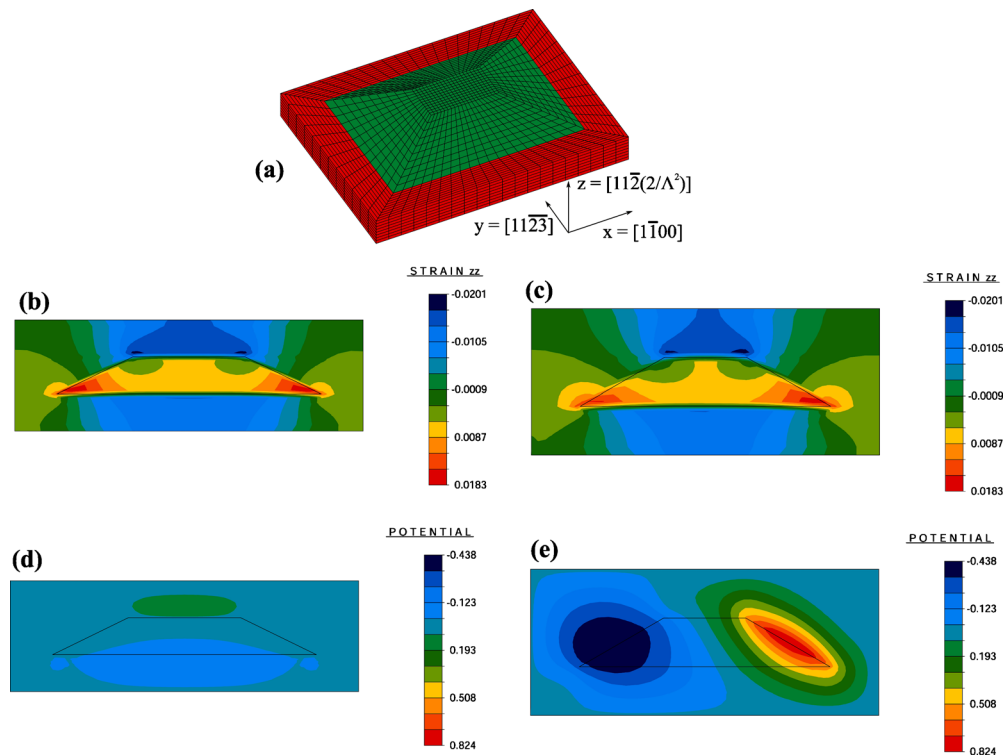
FIG. 10. (Color online) In (a), the FE mesh is shown superimposed on the proposed $(11\bar{2}2)$ QD geometry. The capping layer has been removed for illustrative purposes only. In (b) and (c), the elastic strain distribution is presented in 2D projected contour plots of a QD cross-section through the *xz*- and *yz*-planes, respectively. In (d) and (e), the corresponding distributions of the electrostatic potential (in volt) are presented in 2D projected contour plots.

As shown in Fig. 11(c), the potential drop in the *z*-direction (growth direction) across the center of the QD, defined as the difference between the maximum and minimum values of the polarization potential, was ~0.2 V (corresponding to electric field of 0.4 MV/cm). The maximum potential drop was along the $[1\bar{1}00]$ direction, reaching ~1.3 V (corresponding to electric field of 1.5 MV/cm).

V. ENERGIES OF QD INTERFACES

In Sec. III we have shown that the QD dominant side facets are of $\{10\bar{1}1\}$ and $\{1\bar{2}10\}$ orientation. Moreover, the QDs can nucleate at surface depressions comprising such facets. Under gallium-rich conditions, the nonpolar $\{11\bar{2}0\}$ planes comprise two types of surface atoms, i.e., both nitrogen and gallium,[32] while the $\{10\bar{1}1\}$ surfaces consist of gallium atoms at two distinct types of sites in the surface layer, bonding to one or three nitrogen atoms in the layer below.[33] Theoretical calculations have shown a strong tendency of III-Nitride surfaces to stabilize at reconstructions characterized by the complete absence of nitrogen atoms in the top surface layer,[34] and the stability of the $\{10\bar{1}1\}$ surfaces is further verified by its occurrence in multiple instances such as V-defects, pinholes etc.[19–23]

Our TEM observations indicated that the surface depressions comprising $\{10\bar{1}1\}$ facets tended to be filled by GaN material. In other words, QDs tended to nucleate at such sites, and moreover, these QDs tended to be larger on average than QDs grown on flat $(11\bar{2}2)$ surface. For example, in the 10 ML sample, the QDs sitting on $\{10\bar{1}1\}$ were larger at

their base by ~4 nm on average compared to the ones sitting on the $(11\bar{2}2)$ planes. This prompted us to investigate the energetic stability of the $\{10\bar{1}1\}$ GaN/AlN interface in comparison to $(11\bar{2}2)$. DFT calculations of bicrystalline supercells, using periodic boundary conditions (PBCs), were implemented in order to identify the energetically favorable interfacial configurations.

Calculations were performed using the ABINIT code and Troullier–Martins pseudopotentials.[35,36] The Perdew–Burke–Ernzehof (PBE) generalized gradient approximation was used for the exchange and correlation with an energy cut-off equal to 50 Ry.[37] The Ga 3*d* electrons were treated as core and a nonlinear core correction was implemented. The Brillouin zone was treated by a $4 \times 4 \times 4$ Monkhorst–Pack k-point sampling.[38] For construction of the bicrystalline supercell, AlN was considered unstrained and the normal lattice parameters of GaN were optimized at the imposed AlN in-plane lattice parameters. The epilayer was allowed to relax while the atomic positions of the substrate material (AlN) were kept fixed. It is noted that due to the implementation of PBCs, two nondegenerate interfaces were included in each supercell configuration and they were related by polarity reversal as described in detail elsewhere.[39,40] For each bicrystal, the interfacial energy per unit area was calculated as the excess energy obtained after subtracting the reference energy from the energy of the relaxed configuration. The reference energy corresponded in each case to the sum of the energies of the unstrained AlN and strained GaN crystals that comprised the supercell. The number of atoms was the same in the reference and corresponding relaxed supercells.
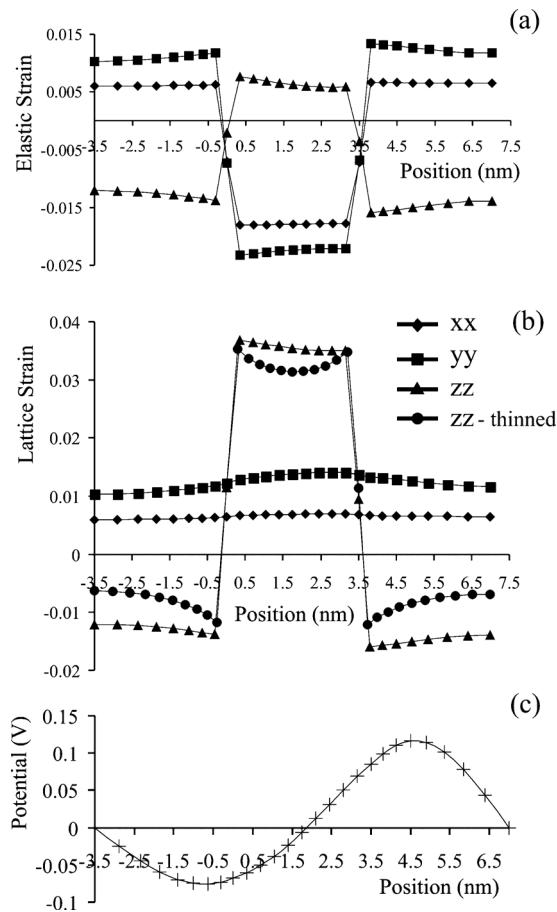
FIG. 11. Quantification of the results of the FE analysis for a cross section through the center of the QD on the *yz*-plane [i.e., (1$\bar{1}$00)]. In (a) and (b), the elastic and lattice normal strain components (ε_{ii}) are given as a function of position along the growth *z*-axis. In (c), the variation in the electrostatic potential with position along the *z*-axis is given.

Based on our calculations the interfacial energy of {10$\bar{1}$1} GaN/AlN was E_{int}=0.046 eV/A^2 while for the {11$\bar{2}$2} GaN/AlN it was almost double, i.e., E_{int}=0.090 eV/A^2. This result verifies that the {10$\bar{1}$1} interfaces are energetically favorable in comparison to the (11$\bar{2}$2) interface. The relaxed interfacial structures are illustrated in Fig. 12.

VI. CONCLUSIONS

In the present contribution we have focused on the structural properties of self-assembled semipolar GaN QDs embedded in (11$\bar{2}$2) AlN grown heteroepitaxially on *m*-plane sapphire by PAMBE. These properties include the morphology and strain distribution, as well as the calculation of their influence on the polarization field. For these purposes CTEM, HRTEM, qHRTEM, and STEM experimental techniques were employed, combined with elastic-electric continuum simulations and DFT energy calculations. Using three projection directions, it has been shown that the QD pyramidal or truncated-pyramidal morphology does not exceed the layer symmetry of the nucleating plane and comprises low energy side facets such as {10$\bar{1}$1} and (11$\bar{2}$0). Due to the roughness of the growth front, QDs also nucleated at
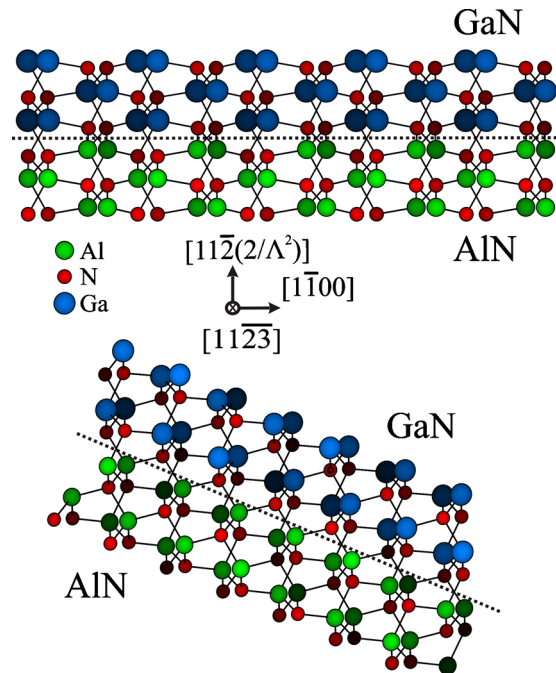

FIG. 12. (Color online) Schematic illustration of the relaxed simulated (11$\bar{2}$2) and {10$\bar{1}$1} interfaces projected along [$\bar{1}\bar{1}$23]. Shading denotes distinct levels along the projection direction. [Λ=(2/3)$^{1/2}$(c/a)].

depressions comprising similar facets. The DFT calculations showed that the {10$\bar{1}$1} interfaces are energetically favorable compared to (11$\bar{2}$2) which explains in terms of interfacial stability the QD nucleation inside surface depressions, and the larger average size of these QDs compared to those sitting on flat (11$\bar{2}$2) surface.

The strain state of the dominant (11$\bar{2}$2)-nucleated QDs was analyzed by combining qHRTEM measurements with FE simulations, and it has been shown to deviate from the biaxial state. The strain analysis showed a nonuniform distribution of strain in the QDs, with larger values toward the QD corners. By solving the elastic-electric problem in a semicoupled manner, it was determined that, despite the larger strain compared to the biaxial state, the potential drop along the growth direction is limited. Furthermore, it is advantageous that the {10$\bar{1}$1} and (11$\bar{2}$0) nanofacets do not localize spatially the electric field. However, one nanofacet, namely, (11$\bar{2}$6), was found to have an adverse effect in this regard. Further work should focus on the elucidation of the influence of the built-in polarization potential on the electron-hole pair and correlation with the PL properties of such nanostructures.

[1]T. Takeuchi, S. Sota, M. Katsuragawa, M. Komori, H. Takeuchi, H. Amano, and I. Akasaki, Jpn. J. Appl. Phys., Part 2 **36**, L382 (1997).

[2]U. T. Schwarz and M. Kneissl, Phys. Status Solidi (RRL) **1**, A44 (2007).

[3]P. Waltereit, O. Brandt, A. Trampert, H. T. Grahn, J. Menniger, M. Ramsteiner, M. Reiche, and K. H. Ploog, Nature (London) **406**, 865 (2000).

[4]S.-M. Hwang, Y. G. Seo, K. H. Baik, I.-S. Cho, J. H. Baek, S. Jung, T. G. Kim, and M. Cho, Appl. Phys. Lett. **95**, 071101 (2009).

[5]J. S. Speck and S. F. Chichibu, MRS Bull. **34**, 304 (2009).

[6]J. Smalc-Koziorowska, G. P. Dimitrakopulos, S.-L. Sahonta, G. Tsiakatouras, A. Georgakilas, and Ph. Komninou, Appl. Phys. Lett. **93**, 021910 (2008).

[7]J. Smalc-Koziorowska, G. Tsiakatouras, A. Lotsari, A. Georgakilas, and G. P. Dimitrakopulos, J. Appl. Phys. **107**, 073525 (2010).

[8]Th. Kehagias, L. Lahourcade, A. Lotsari, E. Monroy, G. P. Dimitrakopulos, and Ph. Komninou, Phys. Status Solidi B **247**, 1637 (2010).

[9]J. M. Gérard, O. Cabrol, and B. Sermage, Appl. Phys. Lett. **68**, 3123 (1996).

[10]J. Renard, P. K. Kandaswamy, E. Monroy, and B. Gayral, Appl. Phys. Lett. **95**, 131903 (2009).

[11]L. Lahourcade, S. Valdueza-Felip, T. Kehagias, G. P. Dimitrakopulos, P. Komninou, and E. Monroy, Appl. Phys. Lett. **94**, 111901 (2009).

[12]S. Schulz, A. Berube, and E. P. O' Reilly, Phys. Rev. B **79**, 081401(R) (2009).

[13]A. Cros, J. A. Budagosky, A. García-Cristóbal, N. Garro, A. Cantarero, S. Founta, H. Mariette, and B. Daudin, Phys. Status Solidi B **243**, 1499 (2006).

[14]S. Founta, C. Bougerol, H. Mariette, B. Daudin, and P. Vennéguès, J. Appl. Phys. **102**, 074304 (2007).

[15]M. J. Hÿtch, J.-L. Putaux, and J.-M. Pénisson, Nature (London) **423**, 270 (2003).

[16]M. J. Hÿtch, E. Snoeck, and R. Kilaas, Ultramicroscopy **74**, 131 (1998).

[17]L. Lahourcade, E. Bellet-Amalric, E. Monroy, M. Abouzaid, and P. Ruterana, Appl. Phys. Lett. **90**, 131909 (2007).

[18]G. P. Dimitrakopulos, Ph. Komninou, and R. C. Pond, Phys. Status Solidi B **227**, 45 (2001).

[19]Y. Chen, T. Takeuchi, H. Amano, I. Akasaki, N. Yamada, Y. Kaneko, and S. Y. Wang, Appl. Phys. Lett. **72**, 710 (1998).

[20]X. H. Wu, C. R. Blass, A. Abare, M. Mack, S. Keller, P. M. Petroff, S. P. DenBaars, J. S. Speck, and S. J. Rosner, Appl. Phys. Lett. **72**, 692 (1998).

[21]O.-H. Nam, M. D. Bremser, B. L. Ward, R. J. Nemanich, and R. F. Davis, Jpn. J. Appl. Phys., Part 2 **36**, L532 (1997).

[22]Th. Kehagias, G. P. Dimitrakopulos, J. Kioseoglou, H. Kirmse, C. Giesen, M. Heuken, A. Georgakilas, W. Neumann, Th. Karakostas, and Ph. Komninou, Appl. Phys. Lett. **95**, 071905 (2009).

[23]Z. Lilienthal-Weber, Y. Chen, S. Ruvimov, and J. Washburn, Phys. Rev. Lett. **79**, 2835 (1997).

[24]Ph. Komninou, J. Kioseoglou, G. P. Dimitrakopulos, Th. Kehagias, and Th. Karakostas, Phys. Status Solidi A **202**, 2888 (2005).

[25]T. D. Young and O. Marquardt, Phys. Status Solidi C **6**, S557 (2009).

[26]O. Marquardt, T. Hickel, and J. Neugebauer, J. Appl. Phys. **106**, 083707 (2009).

[27]K. S. A. Butcher, A. J. Fernandes, P. P.-T. Chen, M. Wintrebert-Fouquet, H. Timmers, S. K. Shrestha, H. Hirshy, R. M. Perks, and B. F. Usher, J. Appl. Phys. **101**, 123702 (2007).

[28]E. Sarigiannidou, E. Monroy, B. Daudin, J. L. Rouviere, and A. D. Andreev, Appl. Phys. Lett. **87**, 203112 (2005).

[29]E. Pan and B. Yang, J. Appl. Phys. **93**, 2435 (2003).

[30]I. Vurgaftman, J. R. Meyer, and L. R. Ram-Mohan, J. Appl. Phys. **89**, 5815 (2001).

[31]P. Dłużewski, G. Maciejewski, G. Jurczak, S. Kret, and J.-Y. Laval, Comput. Mater. Sci. **29**, 379 (2004).

[32]J. E. Northrup and J. Neugebauer, Phys. Rev. B **53**, R10477 (1996).

[33]J. E. Northrup, L. T. Romano, and J. Neugebauer, Appl. Phys. Lett. **74**, 2319 (1999).

[34]J. Neugebauer, Phys. Status Solidi B **227**, 93 (2001).

[35]X. Gonze, J.-M. Beuken, R. Caracas, F. Detraux, M. Fuchs, G.-M. Rignanese, L. Sindic, M. Verstraete, G. Zerah, F. Jollet, M. Torrent, A. Roy, M. Mikami, P. Ghosez, J.-Y. Raty, and D. C. Allan, Comput. Mater. Sci. **25**, 478 (2002).

[36]N. Troullier and J. L. Martins, Phys. Rev. B **43**, 1993 (1991).

[37]J. P. Perdew, K. Burke, and M. Ernzehof, Phys. Rev. Lett. **77**, 3865 (1996).

[38]H. J. Monkhorst and J. D. Pack, Phys. Rev. B **13**, 5188 (1976).

[39]J. Kioseoglou, E. Kalessaki, G. P. Dimitrakopulos, P. Komninou, and T. Karakostas, J. Mater. Sci. **43**, 3982 (2008).

[40]J. Kioseoglou, E. Kalesaki, L. Lymperakis, G. P. Dimitrakopulos, Ph. Komninou, and Th. Karakostas, Phys. Status Solidi A **206**, 1892 (2009).